The energy landscape of adenylate kinase during catalysis

S. Jordan Kerns[1,4,5], **Roman V. Agafonov**[1,5], **Young-Jin Cho**[1,4,5], **Francesco Pontiggia**[1,5], **Renee Otten**[1], **Dimitar V. Pachov**[1], **Steffen Kutter**[1], **Lien A. Phung**[1], **Padraig N. Murphy**[1], **Vu Thai**[1,4], **Tom Alber**[2], **Michael F. Hagan**[3], and **Dorothee Kern**[1]

[1]Howard Hughes Medical Institute, Department of Biochemistry, Brandeis University, Waltham, MA, USA

[2]Department of Molecular & Cell Biology, University of California Berkeley, Berkeley, CA, USA

[3]Department of Physics, Brandeis University, Waltham, MA, USA

Abstract

Kinases perform phosphoryl-transfer reactions in milliseconds; without enzymes, these reactions would take about 8000 years under physiological conditions. Despite extensive studies, a comprehensive understanding of kinase energy landscapes, including both chemical and conformational steps, is lacking. Here we scrutinize the microscopic steps in the catalytic cycle of adenylate kinase, through a combination of NMR measurements during catalysis, pre-steady-state kinetics, MD simulations, and crystallography of active complexes. We find that the Mg^{2+} cofactor activates two distinct molecular events, phosphoryl transfer ($>10^5$-fold) and lid-opening (10^3-fold). In contrast, mutation of an essential active-site arginine decelerates phosphoryl transfer 10^3-fold without substantially affecting lid-opening. Our results highlight the importance of the entire energy landscape in catalysis and suggest that adenylate kinases have evolved to activate key processes simultaneously by precise placement of a single, charged and very abundant cofactor in a pre-organized active site.

INTRODUCTION

Phosphate esters and anhydrides are high-energy linkages that are extremely resistant to nucleophilic attack and are therefore fundamental to genomic stability, long signaling state lifetimes, and storage of biochemical energy[1-4]. While stability is critical, organisms must respond rapidly and effectively to their environment and have therefore evolved enzymes that catalyze transfer of phosphoryl groups with exquisite specificity and enormous rate accelerations relative to the uncatalyzed reaction in solution[5-10]. Impressive progress has been made in understanding protein phosphorylation in cellular processes[11,12] and fundamental work on non-enzymatic phosphoryl transfer (P-transfer) has delivered a deep mechanistic understanding of P-transfer in solution[5-10]; however, a comprehensive understanding of kinase catalyzed phosphorylation is still lacking despite the wealth of literature on many different P-transfer enzymes[5,13]. This includes crystal structures that reveal conservation in the active site and accompanying domain architecture[14]; kinetic studies that establish the rate-limiting steps and the order of events[13]; and NMR that links local fluctuations to global protein dynamics[15,16].

However, catalysis is typically composed of multiple microscopic steps spanning a hierarchy of time and space, which often obscures underlying molecular mechanisms. This has led to persistent controversies, for example about the role of the Mg^{2+} cofactor in kinase catalysis. While some kinases are activated by a single Mg^{2+} ion, additional Mg^{2+} binding may either be required for full activation, result in inhibition, or be involved in structural stabilization[13,17,18]. The variety of different mechanisms attributed to the Mg^{2+} cofactor has resulted in arguments about the kinetic schemes to account for the role of Mg^{2+} in catalysis[19]. Other heated debates focus on the role of conformational changes in the enzymatic reaction[20-25]. Quantitative descriptions of the entire energy landscape of catalysis are necessary to reconcile these different mechanisms including the canonical role of Mg^{2+} in kinase catalysis.

Here we have performed a comprehensive investigation of the adenylate kinase (Adk) energy landscape and have quantified multiple kinetic states along the reaction pathway at atomic resolution. Adk is a ubiquitous and essential phosphoryl-transfer enzyme found in all cells. Adks reversibly transfer a phosphoryl group from ATP to AMP thereby maintaining the equilibrium between cytoplasmic nucleotides (Fig. 1a). During the enzymatic cycle, Adk undergoes large conformational changes by opening/closing of the ATP- and AMP-lid (defined as the protein fragments that close over the Mg-ATP and AMP binding sites, respectively), as visualized in Fig. 1a. Unlike many protein kinases that are activated by protein–protein interactions or covalent modifications[14], Adk is fully active in the presence of its nucleotide substrates and catalyzes a reversible reaction. This provides a tractable framework for a quantitative analysis of the reaction-energy landscape. Using complementary techniques to examine the enzyme during catalysis across many orders of temporal and spatial resolution, we separated the microscopic steps of phosphoryl transfer and conformational motions with pre-steady-state kinetics and NMR dynamics experiments, investigated the mechanism of transition-state stabilization by crystallography and explored the active-site dynamics by molecular dynamics simulation. Combined, these results reveal the major players responsible for the overall rate acceleration and address the key question

of how the enzyme dramatically lowers the energy barrier of P-transfer and accelerates conformational changes essential for both efficient catalysis and suppression of detrimental hydrolysis.

RESULTS

Mg^{2+} as electrostatic "pivot" for phosphoryl transfer

Expanding on previous structural studies and to set the stage for experiments to characterize the free-energy landscape, we obtained a number of Adk crystal structures in multiple biochemical states (e.g., with substrates, with and without metals, and with a transition-state mimic). Many structures of Adks are available that reveal in atomistic detail the conformational cycle between ligand-free and ligand-bound states[26-29]. However, few have been solved with natural substrates in an active quaternary complex, making it difficult to dissect how the enzyme activates P-transfer[16]. Here we present a number of *Aquifex aeolicus* Adk (AAdk) structures bound to natural substrates that have provided mechanistic insight into the catalysis of P-transfer (Table 1). An overlay of many high-resolution snapshots of the AAdk–ADP–ADP ternary complex (AAdk1–4,6) revealed that the transferable phosphoryl group of the donor ADP and its active-site partner R150 show conformational heterogeneity while the acceptor ADP was held rigidly (Fig. 1b). This hinted to movement of only the phosphoryl group of the donor ADP and not the nucleotide acceptor during P-transfer. We note that presenting multiple redundant structures of crystal isoforms is unusual; however, a single structure even with partial occupancy refinement would not illustrate this observed conformational sampling in the active site.

One of the most important components of enzyme-catalyzed P-transfer, the Mg^{2+} cofactor, was not detected in the X-ray structures of the AAdk–ADP–ADP ternary complex despite being present in the mother liquor (Fig. 1b). To obtain a high-resolution structure of AAdk–ADP–ADP with magnesium in the active site, we soaked crystals in the crystallization solution containing 20 mM Mg^{2+} at an elevated pH of 9. A comparison between the structures with and without Mg^{2+} bound showed that they are very similar (Fig. 1c) except for the extra electron density of the Mg^{2+} and its coordination to the six ligands. It is notoriously difficult to distinguish Mg^{2+} from structural water by electron density alone and therefore the position of the Mg^{2+} in the presence of natural substrates is ambiguous in many cases[30]. Consequently, in order to unequivocally determine the position of the metal cofactor in the active site of the enzyme–substrate complex, we also obtained a structure of the ternary AAdk–ADP–ADP complex in the presence of Co^{2+} (AAdk7, Fig. 1d). The position of the cobalt atom derived from anomalous signal collected with the X-ray source at the Co^{2+} edge together with the electron density, was confirmed to be identical to that of Mg^{2+} (AAdk11, Fig. 1d)[31]. Based on these structures, we propose that the metal cofactor helps anchor the flexible donor phosphoryl group for a more favorable attack by the oxygen nucleophile of the acceptor nucleotide.

What happens to the active-site players in the transition state (TS) of the P-transfer reaction? A structure of the AAdk–Mg^{2+}–ADP–AMP quaternary complex with aluminum fluoride as transition-state analogue revealed first that a square planar tetrafluoroaluminate (AlF$_4^-$) and not a neutral AlF$_3$ was in the active site (AAdk8)[32-34]. This agrees with the fundamental

work by Baxter and colleagues on the importance of balancing charge in active sites, a general principle that has been demonstrated for many phosphoryl-transfer enzymes, including β-phosphoglucomutase, phosphoglycerate kinase, protein kinase A, and UMP–CMP kinase[2,35-37]. Second, the AlF_4^- was positioned equidistant between acceptor and donor phosphates due to a 1 Å movement of the latter (Fig. 1e and Supplementary Fig. 1a, b). Third, the Mg^{2+} cofactor was clearly present and maintained its position and coordination partners relative to the AAdk–Mg^{2+}–ADP–ADP quaternary complex (Fig. 1e and Supplementary Fig. 1a,b). The position of the divalent ion (Fig. 1d,e and Supplementary Fig. 1a-c) was identical while the phosphoryl group was transferred between the donor and acceptor sites, suggesting that the Mg^{2+} cofactor acted as an "electrostatic pivot" during P-transfer. In contrast, the active-site R150 shifted in concert with the movement of the phosphoryl group.

Active-site dynamics probed by molecular dynamics simulation

To test our hypothesis that Mg^{2+} helps organize the Adk active-site architecture by positioning the donor and acceptor phosphates in close proximity, we performed 200 ns molecular dynamics (MD) simulations on the closed AAdk–ADP–ADP ternary complex with and without Mg^{2+}.

Simulations with Mg^{2+} showed a stable active-site configuration where both nucleotides experience limited fluctuations (Fig. 2a). Water molecule ligands to the metal ion were also stable and remain coordinated during the simulation (Supplementary Fig. 1c,d). In contrast, simulations in the absence of Mg^{2+} revealed that the active site, and in particular the donor phosphoryl group, samples a much larger distribution of states, (Fig. 2b). These simulations indicate a substantially reduced probability of sampling productive conformations without Mg^{2+}, suggesting an appreciable stabilization of pre-catalytic states by the cofactor [38].

A major challenge for kinases is catalyzing P-transfer efficiently while suppressing the more favorable hydrolysis side reaction. For Adk we measured an extremely slow hydrolysis rate of about $2 \cdot 10^{-6}$ s^{-1} (Fig. 2c) relative to the productive rate of phosphoryl transfer of about $2 \cdot 10^2$ s^{-1}. In comparison to other members of the kinase family with hydrolysis rates in the range of 10^{-2} to 10 s^{-1} [39,40], Adk's ability to execute P-transfer efficiently and avoid unproductive hydrolysis is impressive. From an evolutionary perspective, this striking difference in hydrolysis rates can be rationalized because Adks are abundant proteins that are always active to maintain nucleotide homeostasis whereas many protein kinases are only transiently activated while participating in signaling cascades[11,12].

What possible mechanisms does Adk employ for such efficient suppression of destructive hydrolysis? An obvious way to prevent hydrolysis would be to exclude water from the active site; however, X-ray structures showed that about 20 water molecules were trapped in the AAdk active-site cavity (Fig. 2d). It is likely that these waters helped reduce the energetic penalty associated with de-solvating the highly-charged nucleotide substrates when binding to the active site. Rather than exclude water from the active site to minimize hydrolysis, Adk tightly coordinates these water molecules thereby sequestering them from the phosphoryl groups. The stability of water molecules, present at the same positions in the active site of all crystal structures (AAdk1–11), was investigated in long MD simulations

(Supplementary Figs. 1d and 2 and Movie 1). While the average positions occupied by these water molecules inside the pocket agreed well with those identified in the crystal structures (Fig. 2d), the dynamic behavior of these waters was very different in the presence and absence of Mg^{2+}. Without Mg^{2+}, the waters that are initially present inside the active site exchange with bulk solvent on a timescale of 100 ns. However, in the presence of the metal cofactor the water molecules inside the active-site pocket are prevented from exchanging with bulk solvent throughout the simulations (Supplementary Fig. 2 and Movie 1). The terminal phosphates of the substrates, Mg^{2+}, and the four water molecules coordinating the metal ion form a very stable complex (Supplementary Fig. 1d), serving as a cap to block water exchange. In all simulations we performed (with a combined run time of several microseconds) the water molecules remained tightly coordinated at positions incapable of nucleophilic attack. We note that the discussed points are merely a hypothesis, since hydrolysis happens on the timescale of hours, well beyond the timescales of lid-opening/ closing and the MD regime[41,42].

Dissecting microscopic steps by rapid kinetics experiments

Although Mg^{2+} has minimal impact on the Adk structure (Fig. 1c), it is generally known that Mg^{2+} has an enormous effect on the turnover rate of P-transfer enzymes[5,6,8,13]. To determine the energetic contribution of Mg^{2+} to the overall rate acceleration of P-transfer, we measured turnover rates in the absence of Mg^{2+}.

For all kinetic and NMR experiments described below, we used *Escherichia coli* Adk (EAdk), which has an identical active-site architecture, catalytic mechanism, and rate-limiting steps as AAdk (*cf*. Fig. 3 and Supplementary Fig. 3a-c)[43,44], and higher catalytic efficiency at room temperature. This choice was rooted in the inability to measure conformational dynamics for AAdk by NMR, as explained in the next paragraph. To eliminate traces of divalent metals from solution we included ethylenediaminetetraacetic acid (EDTA) in excess in all metal-free reactions performed (Supplementary Fig. 3d). For EAdk, Mg^{2+} accelerated overall turnover by about five orders of magnitude, in agreement with the general notion that Mg^{2+} is essential for enzyme-catalyzed P-transfer reactions. However, since lid-opening and not P-transfer is rate limiting in the presence of Mg^{2+} [44], the actual rate acceleration of the chemical step by Mg^{2+} must be even greater.

To catch the chemical step directly, we measured the pre-steady-state rate of product formation by quench-flow[13] (Fig. 3 and Supplementary Fig. 3e). With Mg^{2+}, P-transfer on the enzyme was faster than lid-opening, which resulted in an initial burst of product formation as the enzyme completed its first turnover, followed by a linear product increase that was identical to the rate of lid-opening (Fig. 3a). Remarkably, P-transfer was faster than ~500 s^{-1} since the burst phase was completed within the dead time of the instrument (~5 ms). The ratio of the pre-steady-state burst amplitudes reports directly on the on-enzyme equilibrium [EAdk–Mg^{2+}–ADP–ADP]/[EAdk–Mg^{2+}–ATP–AMP] of about 10, with the sum of the two burst amplitudes equal to the total enzyme concentration (Fig. 3a). This is in contrast to the free nucleotide equilibrium of about 1. The values for the on-enzyme nucleotide equilibrium were confirmed by nucleotide saturation experiments (Supplementary Fig. 3f,g). We note that an on-enzyme equilibrium of 10:1 is equivalent to a

small difference in free energy (~1.3 kcal/mol) between the states, which is fully consistent with the idea that optimal enzyme catalytic efficiency is achieved when the free energies of reaction intermediates are balanced[8].

In the absence of Mg^{2+}, P-transfer is severely impaired. In the reverse reaction, no burst phase was observed and the turnover rates were identical between the pre- and steady-state regimes, indicating that P-transfer was rate limiting (Fig. 3c). Unexpectedly, in the forward direction a resolved burst followed by a second phase seemed to imply that a step following P-transfer was also drastically slowed down to about 0.05 s^{-1} without Mg^{2+} (Fig. 3b and Supplementary Fig. 3e).

Mg^{2+} greatly accelerates lid-opening

Could this other slow step in the absence of Mg^{2+} be the lid-opening? ^{15}N-CPMG NMR relaxation dispersion experiments have previously been used to quantify the millisecond lid-opening rates during catalysis in the presence of Mg^{2+} [44]. Strikingly, when we measured EAdk during catalysis without Mg^{2+}, the dispersion profiles were flat (Fig. 4a and Suppl. Note 1), indicating that the rate of lid-opening could be shifted into the slow-exchange regime and thus too slow to be detected. Such NMR relaxation behavior of the enzyme agrees with the rate of lid-opening of 0.05 s^{-1} as determined by pre-steady-state kinetics (Table 2). We note that in the slow-exchange regime, one would expect to see signals for both states in the HSQC spectrum, which we did not observe here for EAdk (Fig. 4b). A plausible explanation for this phenomenon is a small population of the minor, open state that would give rise to weak signals. In addition, the line broadening of signals corresponding to the open state is proportional to the closing rate, which is considerably faster than the opening rate, and could broaden the already weak signals beyond detection. However, the absence of NMR dispersion could also be caused by a lack of motions. To differentiate between these scenarios, we measured the temperature dependence of the NMR relaxation dispersion profiles[45]. For an exchange process that is slow on the NMR timescale, the exchange contribution (R_{ex}) is equal to the lid-opening rate whereas for a fast-exchange process it is inversely proportional to the sum of the lid-opening/closing rate.

We observed an increase in R_{ex} by raising the temperature from 20 to 40 °C, with a uniform amplitude of ~1 s^{-1} for all residues that experience the exchange process (Fig. 4c). When plotted on the structures (Fig. 4d), these residues are very similar to the ones that report on the lid-opening/closing in the presence of magnesium[44]. These results confirm that the lid-opening in the absence of magnesium is indeed slow on the NMR timescale. Consequently, R_{ex} reflects the rate of lid-opening; however, the dispersion data do not provide its accurate value nor information about the closing rate and the relative population of the states. Therefore, we conclude that a second, unexpected role for the Mg^{2+} cofactor is to dramatically accelerate lid-opening by about three orders of magnitude (Table 2).

How can Mg^{2+} lower the activation barriers of the two major steps in the catalytic cycle? We envision that Mg^{2+} simultaneously helps shield the strong electrostatic interactions between active-site arginines and substrates to facilitate lid-opening and correctly orients the active-site players for efficient P-transfer. This suggests that substituting other divalent metals for Mg^{2+} should activate lid-opening similarly while P-transfer might be more

specifically tuned to the charge density of Mg^{2+}. Indeed, we found that P-transfer for all divalent cations other than Mg^{2+} was much slower and, in fact, rate limiting, indicating that the active-site chemistry is optimized for Mg^{2+} (Fig. 5a, Supplementary Fig. 4, Table 2, and Supplementary Table 1). In contrast, the rates of lid-opening/closing measured in the presence of Mg^{2+} and Ca^{2+} were similar (Fig. 5b, Table 2, Supplementary Table 2, and Suppl. Note 2), implying electrostatics as the predominant cause for this strong acceleration of lid-opening. Simple electrostatic potential and interaction energy calculations reveal that the coordination of a divalent cation to the nucleotides opposite to the coordinating arginine side chains weakens the strong electrostatic interactions between the phosphates of the nucleotides and the arginine residues from the lids (Fig. 5c,d). Since these interactions need to be broken for the lids to open, the placement of Mg^{2+} in Adk indeed accelerates lid-opening via electrostatics.

We note that the lid-opening rates of AAdk without Mg^{2+} were too slow to be measured by ^{15}N-CPMG relaxation dispersion experiments[45]; therefore, EAdk was used for all kinetic and NMR experiments.

A conserved arginine accelerates P-transfer 10^3-fold

In an effort to inventory the contribution of other players in lowering the energy barrier of catalysis, we focused our attention on the conserved active-site R150. We have already seen that this residue is flexible and mirrors the donor phosphoryl group position (Fig. 1b). Mutation of R150 has previously been shown to drastically inhibit the rate of enzyme turnover[46]. A comparison between the X-ray crystal structures of wild-type (WT) AAdk (AAdk1) and R150K mutant (AAdk9–10) shows that this mutation disrupts the hydrogen bonding between R150 and the donor β-phosphate. This implies that a specific coordination of the bidentate guanidinium group of the arginine side chain to the transferring phosphoryl group, rather than a positive charge, is needed to position the reactants for catalysis (Fig. 5e,f). By quantifying the change in the P-transfer and lid-opening rates for the EAdk R150K mutant (numbering refers to AAdk, see Supplementary Fig. 3a) we found that this arginine residue has a 10^3-fold effect on P-transfer but negligible effect on lid-opening (Fig. 5g, Supplementary Fig. 5, Table 2, Supplementary Table 2, and Suppl. Notes 3 and 4). The total acceleration from Mg^{2+} and R150 together was therefore larger than 10^8-fold on the rate of P-transfer (Table 2).

DISCUSSION

Our results reveal how Adks accelerate the rate of P-transfer ($k_{chem} > 500$ s^{-1}) by more than 14 orders of magnitude relative to the uncatalyzed reaction ($3.9 \cdot 10^{-12}$ s^{-1})[6] while minimizing the hydrolysis side reaction. We find that Mg^{2+} specifically accelerates P-transfer ($> 10^5$-fold) by reducing non-productive active-site fluctuations (Fig. 2a,b), stabilizing an architecture resembling the TS, and serving as an anchor to the phosphoryl group pivoting between donor and acceptor nucleotides (Fig. 1e). In addition, the Mg^{2+} cofactor accelerated lid-opening (10^3-fold) by weakening the strong electrostatic interactions of the closed quaternary complex (Fig. 5c,d). The multiple catalytic roles for Mg^{2+} is remarkable considering that P-transfer and lid-opening are very different molecular events:

one involves a subtle, 2 Å transfer of a phosphoryl group and the other a large-scale, coordinated motion of domains. In contrast, non-enzymatic P-transfer was only accelerated 10-fold by Mg^{2+} [6], highlighting the evolutionary impact of this highly charged and abundant cation on the enzyme's energy landscape. R150 contributed an additional 10^3-fold acceleration to the phosphoryl-transfer step (Table 2) on top of the large acceleration provided by converting a bimolecular reaction in solution to a unimolecular one with a preferred active-site geometry[47]. Our results rule out a previously proposed mechanism of activation of Adk by direct binding of a second Mg^{2+} [19]; their data can be fully explained by our model and the well-known K_D of Mg^{2+} to nucleotides.

We note that there is extensive literature on Adks, and kinases in general, that can be confusing and contradictory because enzyme catalysis is often reduced to an observed rate constant (k_{cat}/K_M) that is a convolution of multiple reaction steps. This has contributed to mechanistic misinterpretations because critical conformational motions are often hidden and therefore ignored. The importance of characterizing kinase catalysis in molecular detail has been emphasized many times[5,16,46], but has unfortunately lagged far behind our understanding of non-enzymatic P-transfer[5]. Here we have quantified the microscopic states along the Adk energy landscape (Fig. 1a and Table 2) by analyzing the enzyme during catalysis which sheds light onto long-standing controversies and provides a general framework for understanding the role of divalent metals and conformational changes in kinase function[13]. However, we prefer to avoid speculation about associative versus dissociative transition states in enzymatic phosphoryl transfer.

We have characterized the free-energy landscape of catalysis and quantified the energetic contributions of individual players to each microscopic step. Our experiments reveal the catalytic strategies Adks use to both pre-organize the active site for P-transfer and destabilize the quaternary complex for efficient product release. As was elegantly demonstrated by Mayo and collaborators, the principles of reducing unproductive active-site fluctuations and minimizing solvent accessibility is essential to improve the design of enzymes[48]. However, despite remarkable progress[48-51], nature's enzymes remain far superior highlighting the urgent need to understand the entire energy landscape of enzymatic catalysis.

A complete description of the tremendous rate acceleration achieved by biological catalysts continues to be a captivating topic in biology[38,52-55]. A large number of X-ray structures of active complexes, detailed kinetic characterizations, and computational studies on kinases have been reported and may lead to the assumption that little is left to be discovered about kinase function. However, the understanding of free-energy landscapes underlying the impressive acceleration of P-transfer by kinases has been limited. For hydrogen-transfer enzymes, the role of active-site pre-organization and conformational sampling in catalysis has been extensively investigated[38,53-56]. It has been 27 years since Fierke and coworkers quantified the microscopic steps of the dihydrofolate reductase (DHFR) energy landscape[57], and the exquisite distance sensitivity of hydride transfer continues to make this and similar systems attractive for studies of enzyme catalysis[54]. We hope that the comprehensive catalytic framework described here for Adk will provide a similar foundation for understanding the catalytic power of one of the most important classes of enzymes, kinases.

ONLINE METHODS

X-ray crystallography structure determination

For crystallization, *Aquifex aeolicus* adenylate kinase (AAdk1–8,11) and its R150K mutant (AAdk9–10) were expressed and purified as described before [44].

AAdk crystals were grown at 18 or 22 °C with 20–50 mg/mL protein in the following conditions: 20 mM $MgCl_2$, 20 mM ADP, and 25 mM in citric acid at pH 4.6 (AAdk1); 25 mM $MgCl_2$, 25 mM ATP, 25 mM AMP, and 20 mM Tris-HCl at pH 7.4 (AAdk2); 35 mM ADP and 20 mM citric acid at pH 4.6 (AAdk3); 38 mM $MgCl_2$, 38 mM ADP, and 20 mM MES at pH 5.0 (AAdk4); 22 mM AMPPNP and 20 mM MES at pH 5.0 (AAdk5); 15 mM $MgCl_2$, 15 mM ADP, and 20 mM Tris-HCl at pH 7.0 (AAdk6); 17.3 mM ADP, 41.2 mM $CoCl_2$, and 20 mM Tris-HCl at pH 7.4 (AAdk7); 25 mM ADP, 20 mM $MgSO_4$, and 20 mM AlF_x (AAdk8); 20 mM ADP, 20 mM $MgCl_2$, and 20 mM Tris-HCl at pH 7.0 (AAdk9–11). All complexes were mixed with the crystallization solution that contains 0.1 M sodium acetate trihydrate (pH 4.6), 0.2 M ammonium acetate, and 30% (w/v) polyethylene glycol 4000 in a 1:1 (v/v) ratio.

During the growth of AAdk5 crystals with AMPPNP, the AMPPNP analogue hydrolyzed to AMPPN. Since the electron density of AMPPN's nitrogen is indistinguishable from the density of ADP's oxygen, we used ADP for modeling. For AAdk8 crystals, AAdk was premixed with ADP and incubated for one week before addition of 20 mM $MgSO_4$ and AlF_x [from the mixture of $Al(NO_3) \cdot 9\ H_2O$ and NaF]. After another day of incubation, crystal trays were set up with aforementioned conditions and crystals were grown for another week. We note that this structure has a minor occupancy of ADP–ADP in the active site, but due to low occupancy we did not refine it further and only Mg^{2+}–ADP–AMP–AlF_4^- was used for modeling. For AAdk11, crystals were soaked in crystallization solution where the pH had been raised to pH 9 after the addition of 20 mM Mg^{2+}. We note that for AAdk11 there is ~25% AMP occupancy in the AMP lid.

Diffraction data were collected at 100 K at the Advanced Light Source (Lawrence Berkeley National Laboratory) beamline 8.2.1 for AAdk2–3,5, 8–11 and beamline 8.2.2 for AAdk4,6–7. Diffraction data for AAdk1 were collected at 100 K at and the Advanced Photon Source beamline 23ID-B. The details of the data collection are listed in Table 1.

Data were processed, scaled, phased, and refined using iMOSFLM [58], Scala [59], Phaser [60], and REFMAC5 [61] in CCP4 [62]. The space groups were determined by Pointless[59] and are identical for all data sets: P212121. The AAdk structure (PDB 2RGX[43]) without ligand was used as the search model for molecular replacement. Initial refinement was carried out, followed by manual rebuilding in Coot [63,64], and further iterative refinements were carried out using PHENIX [65] (except for AAdk11 where REFMAC5 was used). Hydrogen atoms were added and refined as isotropic for the AAdk1 and AAdk8 models while other models do not include protons. For data sets with an atomic resolution better than 1.7 Å (except for AAdk11), the individual anisotropic ADP refinement method was applied. The final structural models of each data set were validated using the tools available in PHENIX

(phenix.model_vs_data) [66] or CCP4. The collection wavelengths for AAdk1–6,8–11 were between 0.973900 and 1.00001 Å.

For AAdk1–6 and AAdk8–11, there were no residues in the disallowed regions of the Ramachandran plot while the lowest percentage of favorable Ramachandran angles was 98.76% for AAdk6. The highest percentage of rotamer outlier for these data sets was also for AAdk6 with 2.26% of residues.

For AAdk7 crystals, the diffraction data were collected at the Cobalt absorption edge (λ=1.608600 Å). The anomalous scattering was identified by running Phaser-EP in PHENIX. In MR-SAD phasing mode, a refined protein model from Phaser and REFMAC5 was used as partial model for detecting the anomalous peak positions. The anomalous difference map confirms the location of cobalt in the active site. Not only Co^{2+} atoms, but also the location of the P and S atoms could be confirmed and are consistent with anomalous scattering at this wavelength. While fixing the Co^{2+} atom based on the anomalous peak position, further refinements were carried out. The occupancy of cobalt was not full, albeit cobalt in the active site of chain A displayed anomalous scattering up to 17 sigma level. The anomalous multiplicity for the AAdk7 refinement was 7.2 (6.7) and the anomalous completeness was 99.4% (96.4%). For this data set, 0.74% and 96.03% of residues were in the disallowed and favorable regions of the Ramachandran plot, respectively. In addition, 4.53% of AAdk7 residues were in rotamer outlier configurations.

For AAdk11 crystals, the presence of Mg^{2+} in the active site of chain B was established from the electron density and in addition from the perfect six-fold coordination of nearby water molecules and the nucleotides. Moreover, the Mg^{2+} position is in agreement with the position in the AAdk8 structure and the anomalous density in the Aadk7 Co^{2+}-structure. We note that there is partial occupancy of ~25% AMP in the donor site in chain B. In chain A, we did not model a Mg^{2+} as little electron density is seen in this site and the coordination to the nearby water molecules is not perfect, very similar to what is observed in the crystal structures AAdk1–8 where no Mg^{2+} is present.

Structural alignments were done using maximum likelihood algorithms implemented in the program "theseus", which produces more accurate results compared to conventional least-square criteria[67].

Molecular Dynamics Simulations

The A molecule of the AAdk1 crystal structure (see Table 1) in complex with two ADP molecules was used as an initial model for all atom classical molecular dynamics (MD) simulations. Parameterization was performed with the CHARMM 22-protein all-atom force field with the CMAP backbone energy correction included [68,69] using the program CHARMM [70]. The parameters for the bound ADP molecules, singly protonated on the terminal phosphates, were derived by combining parameters for a fully charged ADP and for inorganic phosphate $PO_4H_2^-$ included in the standard force field [71]. The system was solvated in a truncated octahedral TIP3P [72] water box using the software Solvate (http://www.mpibpc.mpg.de/home/grubmueller/downloads/solvate/index.html) and CHARMM [70].

Note on the choice of a classical treatment for the active site: a complete quantitative understanding of the impact of the magnesium ion on the catalyzed reaction may require an accurate quantum-mechanical description of the active site region [73-76]. However, the size of the system, the timescale of the dynamical properties under study, and the difficulties in the characterization of precise structural and geometrical properties of the active site in terms of the magnesium ion positioning and protonation states of the ADP nucleotides, make a direct quantum-mechanical approach infeasible without a previous mechanistic exploration at classical level [77,78]. Furthermore, even though the classical nonpolarizable force-fields with fixed atom charges have limited accuracy, they have been successfully applied to similar metal ion and/or nucleotide dependent problems [79-81]. A quantitative QM investigation of the catalyzed chemical step of the phosphoryl-transfer reaction is currently underway, but it is beyond the scope of the present study.

The simulation boxes for both systems, with and without the Mg^{2+} ion in the active site, were neutralized and then 50 mM NaCl was added using CHARMM [70]. The solvated structures were minimized with the Conjugate Gradient method as implemented in NAMD 2.7b2 [82], and then gradually heated to 300 K with a time step of 1 fs while gradually releasing positional restraints in a MD simulation of 2 ns. Periodic boundary conditions were applied to the simulation cell. Electrostatics were treated with the Particle Mesh Ewald scheme [83]. The bonds of all hydrogens were constrained with the SHAKE algorithm [84]. The structures were equilibrated for an additional 20 ns in the NPT ensemble (T = 300 K, P = 1.01325 bar) with the software NAMD 2.7b2. The temperature was controlled with the Langevin dynamics method [85] while keeping the pressure constant using the combined Langevin piston Nose-Hoover method [86,87] as implemented in NAMD 2.7b2.

Equilibrated structures were then converted to GROMACS 4.5.3 [88] using a set of in-house scripts. For each of the two setups, with and without the Mg^{2+} ion bound to the active site, four independent replicas of 100 ns each were simulated in the NPT ensemble (T = 300 K,P = 1.01325 bar), constraining the hydrogen bond lengths with LINCS [89] and constraining the TIP3P waters with SETTLE[90]. The temperature was controlled with the Nose-Hoover thermostat [91,92] and pressure was controlled with the Parrinello-Rahman pressure coupling [93,94], as implemented in GROMACS 4.5.3. Four of the trajectories were further extended to 200 ns.

To define the protein cavities during the analysis of the water dynamics (see Fig. 2d and Supplementary Fig. 2) we used an algorithm based on the clustering of the alpha spheres [95] implemented in Fpocket [96]. Fpocket relies on the Voronoi tassellation of space implemented in the software Qvoronoi (http://www.qhull.org/). The volume of the cavity and the water molecules present inside those cavities were determined using a set of scripts that can partition a complex geometry by defining a convex hull based on atomic positions (kindly provided by Dr. Patrick Varilly [97]).

The calculations of the electrostatic potential (see Fig. 5c) have been performed using the software APBS [98] using the interface built into VMD 1.9 [99]. The linearized form of the Poisson-Boltzmann equation (LPBE) at 298.15 K was solved, placing the protein in a cubic box of size 80 Å and 129 grid points in each dimension. The solvent dielectric constant was

set to 78.54. To account for the solution buffer, 50 mM monovalent positive and negative mobile ions were included in the calculation.
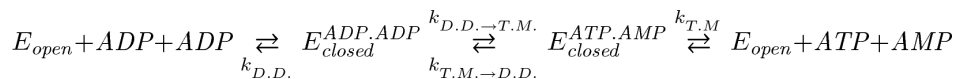
All trajectories were analyzed with the software VMD 1.9 [99]. The software Grace (http://plasma-gate.weizmann.ac.il/Grace) was used for the plots and Tachyon ray tracer (built into VMD 1.9, http://jedi.ks.uiuc.edu/~johns/raytracer) for the molecular renderings.

Pre-steady-state kinetics measurements

Pre-steady-state kinetics was measured using a 3-syringe rapid quench-flow apparatus RQF-3 (KinTek Corp). Protein solution was loaded into one of the syringes, nucleotides (ADP or AMP+ATP mixture with or without divalent ions) into the second syringe and quench solution (30% TCA + 6 M HCl mixture) was loaded into the third syringe. The reaction was initiated by a simultaneous push of all 3 syringes by a high-precision servo-motor. Required delay between the initial mixing of the regent and the following quench with acid was achieved by selecting aging loops of different length (which increases the path length for the acid component thus delaying the quench). The forward and reverse reactions were initiated by mixing ADK with AMP and ATP or ADP, respectively. The protein concentration in the syringe (before mixing) was varied between 40 and 1000 μM while the nucleotide concentration (in the syringe) was 8–32 mM, depending on the experiment. The buffer contained 100 mM Tris (pH 7.0), 80 mM KCl, and equimolar (with total concentration of nucleotides) concentration of Mg^{2+} or 50 mM EDTA. The temperature was controlled with a circulating water bath Isotemp 2150 Nano (Fisher Scientific) set to 25 °C unless specified otherwise.

The amount of product was quantified using high-pressure liquid chromatography (HPLC). Protein precipitated by quench was separated using Spin-X centrifugal tube filters (Costar), filtered supernatant was diluted to avoid HPLC detector saturation, and pH was brought to 6.0 to achieve optimal separation. The samples were analyzed on an HPLC system (Agilent Infinity 1260) with a high precision autosampler (injection error <0.1 μL), analytical HPLC column ACE (i.d. 2.4 mm, length 250 mm, C18-AR, 5 Å pore-size) and separated using isocratic elution with potassium phosphate mobile phase (100 μM, pH 6.0). Control experiments were performed to determine residual contamination in the commercially purchased ADP, ATP, and AMP stocks.

The rate constants of the phosphoryl transfer in the forward and reversed direction ($k_{T.M.\rightarrow D.D.}$ and $k_{D.D.\rightarrow T.M.}$, respectively) reported in Table 2 were calculated considering a) the exponential phase of the forward reaction $E^{ATP.AMP} \rightarrow E^{ADP.ADP}$, which is determined by the sum of the constants $k_{T.M.\rightarrow D.D.} + k_{D.D.\rightarrow T.M.}$ and b) the on-enzyme equilibrium which gives the ratio between two the constants ($k_{T.M.\rightarrow D.D.}$) / ($k_{D.D.\rightarrow T.M.}$).

$$E_{open}+ADP+ADP \underset{k_{D.D.}}{\overset{}{\rightleftarrows}} E_{closed}^{ADP.ADP} \underset{k_{T.M.\rightarrow D.D.}}{\overset{k_{D.D.\rightarrow T.M.}}{\rightleftarrows}} E_{closed}^{ATP.AMP} \overset{k_{T.M}}{\rightleftarrows} E_{open}+ATP+AMP$$

Lid-opening in the forward direction (opening out of the $E^{ADP.ADP}$ state) can be determined directly from the slope of the linear phase in Fig. 3b, since the equilibrium is highly skewed towards $E^{ADP.ADP}$ state.

Lid-opening in the reverse direction (opening out of the $E^{ATP.AMP}$ state) cannot be directly read from the slope in Fig. 3c, since in this direction phosphoryl transfer is rate-limiting. Instead, one can calculate the lid-opening rate constant from the observed rate of phosphoryl transfer after accounting for the probabilities of opening and going back into $E^{ADP.ADP}$ state. The rate constant can be calculated from the observed rate constant according to the following equation:

$$k^{obs}_{ADP.ADP \rightarrow ATP.AMP} = k_{ADP.ADP \rightarrow ATP.AMP} \cdot \frac{k^{open}_{ATP.AMP}}{k^{open}_{ATP.AMP} + k_{ATP.AMP \rightarrow ADP.ADP}}$$

Time-correction procedure for very fast kinetics in the quench-flow experiments

Data obtained in the presence of Mg^{2+}, Ca^{2+}, or Co^{2+} (very fast kinetics) displayed unphysical amplitudes of the burst phase. The apparent amplitude was greater than the enzyme concentration, which indicated a discrepancy between the real quench delay and the delay value specified in the instrument. To take into account this apparent dead time of the instrument, data were corrected, using quenched-flow experiments performed in the forward and reverse directions. Instrumental delay calculations were based on the fact that the sum of the pre-steady-state bursts for forward and reversed reactions must be equal to the total enzyme concentration.

Experimental bursts can be found as:

$$\begin{aligned} A'_+ &= A_+ + k_+ \cdot t_d \\ A'_- &= A_- + k_- \cdot t_d, \end{aligned}$$

where $A'_\pm$ are experimentally measured bursts in the forward and reverse direction, $k_\pm$ are kinetic rates in the forward and reverse direction, and $A_\pm$ are «true» bursts in the forward and reverse direction.

Thus the delay time t_d is

$$t_d = [(A'_+ + A'_-) - (A_+ + A_-)]/[k_+ + k_-] = [(A'_+ + A'_-) - 1]/[k_+ + k_-]$$

Finally, the true experimental delay in the experimental data can be calculated as

$$t = t' + t_d,$$

where t' is a delay without the dead-time correction.

All values reported in Table 2 were obtained from individual fits. Consistent results are also obtained through global fitting using KinTek Explorer, linking the values of all rate constants among the data sets including the values from in-solution and on-enzyme nucleotide equilibrium.

NMR Dynamics

^{15}N-TROSY CPMG relaxation dispersion experiments [100] were collected on either Varian Inova 500 or 600 MHz or Bruker Avance 800 MHz (cryo-probe) spectrometers. Adk concentrations were usually 2 mM. Substrate saturation of Adk was achieved with 20 mM ADP in 100 mM HEPES, 50 mM NaCl (pH 7.0) and 5 mM TCEP. The concentration of divalent metal used in CPMG dispersion experiments was kept equimolar with the concentration of ADP. Sample measured in the absence of divalent metals were conducted in the presence of 5 mM EDTA.

Typical parameters for ^{15}N-TROSY CPMG relaxation dispersion experiments were a 40 millisecond constant-time period; 2 second delay between transients; 12 different refocusing field strengths from 50 – 1000 Hz collected interleaved; with 1024 and 128 direct and indirect points, respectively; and 25 °C. For experiments conducted at 30 °C and 40 °C, the constant-time period was increased to 60 and 72 milliseconds, respectively.

Standard [^{1}H-^{15}N]-TROSY-HSQCs were always collected before and after the CPMG experiment to check sample stability. CPMG experiments usually took 2.5 days to complete. ^{15}N-CPMG dispersions collected on the Avance 800 MHz were collected as downfield and upfield pairs to minimize off-resonance effects for the larger sweep-width and for lower ^{15}N pulse powers required on cryoprobes.

Data was processed using the NMRPipe software suite [101] and visualized by either CCPN or NMRViewJ [102,103]. Relaxation-dispersion profiles were calculated from peak intensities and analyzed with the general Carver-Richards equation for two-site exchange with in-house scripts [104-107]. Uncertainties were estimated from the average variation in dispersion for residues not experiencing exchange together with the signal-to-noise ratio of each resonance to be analyzed. Global fit uncertainties were estimated by a jackknife method.

Steady-State Kinetics Measurements

Steady-state kinetics measurements were collected with 4 mM ADP and equimolar (with nucleotide) concentrations of divalent metal. The enzyme concentration was varied between 0.5 nM to 25 nM; buffer was 100 mM HEPES (pH 7.0) and 80 mM KCl; measurements were collected at room temperature. The amount of product produced over 16 min was quantified using high-pressure liquid chromatography (HPLC) as described above for pre-steady-state kinetics.

Supplementary Material

Refer to Web version on PubMed Central for supplementary material.

REFERENCES FOR MAIN TEXT

1. Westheimer FH. Why nature chose phosphates. Science. 1987; 235:1173–1178. [PubMed: 2434996]

2. Bowler MW, Cliff MJ, Waltho JP, Blackburn GM. Why did Nature select phosphate for its dominant roles in biology? New Journal of Chemistry. 2010; 34:784–794.

3. Schroeder GK, Lad C, Wyman P, Williams NH, Wolfenden R. The time required for water attack at the phosphorus atom of simple phosphodiesters and of DNA. Proceedings of the National Academy of Sciences of the United States of America. 2006; 103:4052–4055. [PubMed: 16537483]

4. Kamerlin SC, Sharma PK, Prasad RB, Warshel A. Why nature really chose phosphate. Q Rev Biophys. 2013; 46:1–132. [PubMed: 23318152]

5. Lassila JK, Zalatan JG, Herschlag D. Biological phosphoryl-transfer reactions: understanding mechanism and catalysis. Annu Rev Biochem. 2011; 80:669–702. [PubMed: 21513457]

6. Stockbridge RB, Wolfenden R. The Intrinsic Reactivity of ATP and the Catalytic Proficiencies of Kinases Acting on Glucose, N-Acetylgalactosamine, and Homoserine A THERMODYNAMIC ANALYSIS. Journal of Biological Chemistry. 2009; 284:22747–22757. [PubMed: 19531469]

7. Jencks, WP. Catalysis in chemistry and enzymology. Dover, New York: 1987. p. xvi-836.

8. Knowles JR. Enzyme-catalyzed phosphoryl transfer reactions. Annual Review of Biochemistry. 1980; 49:877–919.

9. Cleland WW, Hengge AC. Enzymatic mechanisms of phosphate and sulfate transfer. Chemical Reviews. 2006; 106:3252–3278. [PubMed: 16895327]

10. Thatcher GRJ, Kluger R. Mechanism and Catalysis of Nucleophilic-Substitution in Phosphate-Esters. Advances in Physical Organic Chemistry. 1989; 25:99–265.

11. Hunter T. Tyrosine phosphorylation: thirty years and counting. Curr Opin Cell Biol. 2009; 21:140–146. [PubMed: 19269802]

12. Jura N, et al. Catalytic control in the EGF receptor and its connection to general kinase regulatory mechanisms. Mol Cell. 2011; 42:9–22. [PubMed: 21474065]

13. Adams JA. Kinetic and catalytic mechanisms of protein kinases. Chemical Reviews. 2001; 101:2271–90. [PubMed: 11749373]

14. Endicott JA, Noble ME, Johnson LN. The structural basis for control of eukaryotic protein kinases. Annu Rev Biochem. 2012; 81:587–613. [PubMed: 22482904]

15. Henzler-Wildman K, Lei M, Thai V, Karplus M, Kern D. A hierarchy of timescales in protein dynamics linked to enzyme catalysis. 2007

16. Masterson LR, et al. Dynamics connect substrate recognition to catalysis in protein kinase A. Nat Chem Biol. 2010; 6:821–8. [PubMed: 20890288]

17. Mukherjee K, Sharma M, Jahn R, Wahl MC, Sudhof TC. Evolution of CASK into a Mg2+-Sensitive Kinase. Science Signaling. 2010; 3

18. Bao ZQ, Jacobsen DM, Young MA. Briefly Bound to Activate: Transient Binding of a Second Catalytic Magnesium Activates the Structure and Dynamics of CDK2 Kinase for Catalysis. Structure. 2011; 19:675–690. [PubMed: 21565702]

19. Tan YW, Hanson JA, Yang H. Direct Mg2+ binding activates adenylate kinase from Escherichia coli. J Biol Chem. 2009; 284:3306–13. [PubMed: 19029291]

20. Bhabha G, et al. Divergent evolution of protein conformational dynamics in dihydrofolate reductase. Nat Struct Mol Biol. 2013; 20:1243–9. [PubMed: 24077226]

21. Bhabha G, et al. A dynamic knockout reveals that conformational fluctuations influence the chemical step of enzyme catalysis. Science. 2011; 332:234–8. [PubMed: 21474759]

22. Kamerlin SCL, Warshel A. At the dawn of the 21st century: Is dynamics the missing link for understanding enzyme catalysis? Proteins: Structure, Function, and Bioinformatics. 2009; 9999

23. Adamczyk AJ, Cao J, Kamerlin SC, Warshel A. Catalysis by dihydrofolate reductase and other enzymes arises from electrostatic preorganization, not conformational motions. Proc Natl Acad Sci U S A. 2011; 108:14115–20. [PubMed: 21831831]

24. Nagel ZD, Klinman JP. A 21st century revisionist's view at a turning point in enzymology. Nature Chemical Biology. 2009; 5:543–550. [PubMed: 19620995]

25. Klinman JP, Kohen A. Hydrogen tunneling links protein dynamics to enzyme catalysis. Annu Rev Biochem. 2013; 82:471–96. [PubMed: 23746260]

26. Muller CW, Schlauderer GJ, Reinstein J, Schulz GE. Adenylate kinase motions during catalysis: An energetic counterweight balancing substrate binding. Structure. 1996; 4:147–156. [PubMed: 8805521]

27. Muller CW, Schulz GE. Structure of the Complex between Adenylate Kinase from Escherichia-Coli and the Inhibitor Ap5a Refined at 1.9 Å Resolution - a Model for a Catalytic Transition-State. Journal of Molecular Biology. 1992; 224:159–177. [PubMed: 1548697]

28. Berry MB, Bae EY, Bilderback TR, Glaser M, Phillips GN. Crystal structure of ADP/AMP complex of Escherichia coli adenylate kinase. Proteins-Structure Function and Bioinformatics. 2006; 62:555–556.

29. Berry MB, et al. The Closed Conformation of a Highly Flexible Protein - the Structure of Escherichia-Coli Adenylate Kinase with Bound AMP and AMPPNP. Proteins-Structure Function and Genetics. 1994; 19:183–198.

30. Cowan JA. Metal Activation of Enzymes in Nucleic Acid Biochemistry. Chemical Reviews. 1998; 98:1067–1088. [PubMed: 11848925]

31. Kladova AV, et al. Cobalt-, zinc- and iron-bound forms of adenylate kinase (AK) from the sulfate-reducing bacterium Desulfovibrio gigas: purification, crystallization and preliminary X-ray diffraction analysis. Acta Crystallogr Sect F Struct Biol Cryst Commun. 2009; 65:926–9.

32. Wittinghofer A. Signaling mechanistics: aluminum fluoride for molecule of the year. Curr Biol. 1997; 7:R682–5. [PubMed: 9382787]

33. Coleman DE, et al. Structures of active conformations of Gi alpha 1 and the mechanism of GTP hydrolysis. Science. 1994; 265:1405–12. [PubMed: 8073283]

34. Sondek J, Lambright DG, Noel JP, Hamm HE, Sigler PB. GTPase mechanism of Gproteins from the 1.7-Å crystal structure of transducin alpha-GDP-AIF-4. Nature. 1994; 372:276–9. [PubMed: 7969474]

35. Cliff MJ, et al. Transition state analogue structures of human phosphoglycerate kinase establish the importance of charge balance in catalysis. J Am Chem Soc. 2010; 132:6507–16. [PubMed: 20397725]

36. Baxter NJ, et al. Atomic details of near-transition state conformers for enzyme phosphoryl transfer revealed by rather than by phosphoranes. Proceedings of the National Academy of Sciences. 2010; 107:4555.

37. Baxter NJ, et al. Anionic charge is prioritized over geometry in aluminum and magnesium fluoride transition state analogs of phosphoryl transfer enzymes. J Am Chem Soc. 2008; 130:3952–8. [PubMed: 18318536]

38. Warshel A, et al. Electrostatic basis for enzyme catalysis. Chemical Reviews. 2006; 106:3210–35. [PubMed: 16895325]

39. Armstrong RN, Kondo H, Kaiser ET. Cyclic AMP-dependent ATPase activity of bovine heart protein kinase. Proc Natl Acad Sci U S A. 1979; 76:722–5. [PubMed: 218218]

40. Prowse CN, Lew J. Mechanism of activation of ERK2 by dual phosphorylation. Journal of Biological Chemistry. 2001; 276:99–103. [PubMed: 11016942]

41. Wang Y, Gan L, Wang E, Wang J. Exploring the dynamic functional landscape of adenylate kinase modulated by substrates. J Chem Theory Comput. 2012; 9:84–95. [PubMed: 26589012]

42. Gur M, Madura JD, Bahar I. Global transitions of proteins explored by a multiscale hybrid methodology: application to adenylate kinase. Biophys J. 2013; 105:1643–52. [PubMed: 24094405]

43. Henzler-Wildman KA, et al. Intrinsic motions along an enzymatic reaction trajectory. Nature. 2007; 450:838–44. [PubMed: 18026086]

44. Wolf-Watz M, et al. Linkage between dynamics and catalysis in a thermophilic-mesophilic enzyme pair. Nature Structural & Molecular Biology. 2004; 11:945–949.

45. Palmer AG. NMR characterization of the dynamics of biomacromolecules. Chemical Reviews. 2004; 104:3623–3640. [PubMed: 15303831]

46. Yan HG, Tsai MD. Nucleoside monophosphate kinases: Structure, mechanism, and substrate specificity. Advances in Enzymology. 1999; 73:103.

47. Page MI, Jencks WP. Entropic contributions to rate accelerations in enzymic and intramolecular reactions and the chelate effect. Proc Natl Acad Sci U S A. 1971; 68:1678–83. [PubMed: 5288752]

48. Privett HK, et al. Iterative approach to computational enzyme design. Proc Natl Acad Sci U S A. 2012; 109:3790–5. [PubMed: 22357762]

49. Rothlisberger D, et al. Kemp elimination catalysts by computational enzyme design. Nature. 2008; 453:190–5. [PubMed: 18354394]

50. Kiss G, Celebi-Olcum N, Moretti R, Baker D, Houk KN. Computational enzyme design. Angew Chem Int Ed Engl. 2013; 52:5700–25. [PubMed: 23526810]

51. Blomberg R, et al. Precision is essential for efficient catalysis in an evolved Kemp eliminase. Nature. 2013; 503:418–21. [PubMed: 24132235]

52. Schwartz SD, Schramm VL. Enzymatic transition states and dynamic motion in barrier crossing. Nat Chem Biol. 2009; 5:551–8. [PubMed: 19620996]

53. Benkovic SJ, Hammes-Schiffer S. A perspective on enzyme catalysis. Science. 2003; 301:1196–202. [PubMed: 12947189]

54. Klinman JP. An integrated model for enzyme catalysis emerges from studies of hydrogen tunneling. Chem Phys Lett. 2009; 471:179–193. [PubMed: 20354595]

55. Boehr DD, Dyson HJ, Wright PE. An NMR perspective on enzyme dynamics. Chemical Reviews. 2006; 106:3055–79. [PubMed: 16895318]

56. Rozovsky S, McDermott AE. The time scale of the catalytic loop motion in triosephosphate isomerase. Journal of Molecular Biology. 2001; 310:259–70. [PubMed: 11419951]

57. Fierke CA, Johnson KA, Benkovic SJ. Construction and evaluation of the kinetic scheme associated with dihydrofolate reductase from Escherichia coli. Biochemistry. 1987; 26:4085–92. [PubMed: 3307916]

58. Battye TG, Kontogiannis L, Johnson O, Powell HR, Leslie AG. iMOSFLM: a new graphical interface for diffraction-image processing with MOSFLM. Acta Crystallogr D Biol Crystallogr. 2011; 67:271–81. [PubMed: 21460445]

59. Evans P. Scaling and assessment of data quality. Acta Crystallogr D Biol Crystallogr. 2006; 62:72–82. [PubMed: 16369096]

60. McCoy AJ, et al. Phaser crystallographic software. J Appl Crystallogr. 2007; 40:658–674. [PubMed: 19461840]

61. Murshudov GN, et al. REFMAC5 for the refinement of macromolecular crystal structures. Acta Crystallogr D Biol Crystallogr. 2011; 67:355–67. [PubMed: 21460454]

62. Winn MD, et al. Overview of the CCP4 suite and current developments. Acta Crystallogr D Biol Crystallogr. 2011; 67:235–42. [PubMed: 21460441]

63. Emsley P, Cowtan K. Coot: model-building tools for molecular graphics. Acta Crystallogr D Biol Crystallogr. 2004; 60:2126–32. [PubMed: 15572765]

64. Emsley P, Lohkamp B, Scott WG, Cowtan K. Features and development of Coot. Acta Crystallogr D Biol Crystallogr. 2010; 66:486–501. [PubMed: 20383002]

65. Adams PD, et al. PHENIX: a comprehensive Python-based system for macromolecular structure solution. Acta Crystallogr D Biol Crystallogr. 2010; 66:213–21. [PubMed: 20124702]

66. Afonine PV, et al. phenix.model_vs_data: a high-level tool for the calculation of crystallographic model and data statistics. J Appl Crystallogr. 2010; 43:669–676. [PubMed: 20648263]

67. Theobald DL, Steindel PA. Optimal simultaneous superpositioning of multiple structures with missing data. Bioinformatics. 2012; 28:1972–1979. [PubMed: 22543369]

68. MacKerell AD, et al. All-atom empirical potential for molecular modeling and dynamics studies of proteins. Journal of Physical Chemistry B. 1998; 102:3586–3616.

69. MacKerell A, Banavali N, Foloppe N. Development and current status of the CHARMM force field for nucleic acids. Biopolymers. 2000; 56:257–265. [PubMed: 11754339]

70. Brooks BR, et al. Charmm - a Program for Macromolecular Energy, Minimization, and Dynamics Calculations. Journal of Computational Chemistry. 1983; 4:187–217.

71. Pavelites J, Gao J, Bash PA, Mackerell AD. A molecular mechanics force field for NAD(+), NADH, and the pyrophosphate groups of nucleotides. Journal of Computational Chemistry. 1997; 18:221–239.

72. Price DJ, Brooks CL. A modified TIP3P water potential for simulation with Ewald summation. Journal of Chemical Physics. 2004; 121:10096–10103. [PubMed: 15549884]

73. Gresh N, et al. Analysis of the Interactions Taking Place in the Recognition Site of a Bimetallic Mg(II)-Zn(II) Enzyme, Isopentenyl Diphosphate Isomerase. A Parallel Quantum-Chemical and Polarizable Molecular Mechanics Study. Journal of Physical Chemistry B. 2010; 114:4884–4895.

74. Pontikis G, Borden J, Martinek V, Florian J. Linear Energy Relationships for the Octahedral Preference of Mg, Ca and Transition Metal Ions. Journal of Physical Chemistry A. 2009; 113:3588–3593.

75. Yang SY, et al. Whether proton transition to the triphosphate tail of ATP occurs at protein kinase environment: A car-parrinello ab initio molecular dynamics study. International Journal of Quantum Chemistry. 2008; 108:1239–1245.

76. Peters MB, et al. Structural Survey of Zinc Containing Proteins and the Development of the Zinc AMBER Force Field (ZAFF). J Chem Theory Comput. 2010; 6:2935–2947. [PubMed: 20856692]

77. Ditzler M, Otyepka M, Sponer J, Walter NG. Molecular Dynamics and Quantum Mechanics of RNA: Conformational and Chemical Change We Can Believe In. Accounts of Chemical Research. 2010; 43:40–47. [PubMed: 19754142]

78. Banas P, Jurecka P, Walter N, Sponer J, Otyepka M. Theoretical studies of RNA catalysis: Hybrid QM/MM methods and their comparison with MD and QM. Methods. 2009; 49:202–216. [PubMed: 19398008]

79. Venkatramani R, Radhakrishnan R. Computational study of the force dependence of phosphoryl transfer during DNA synthesis by a high fidelity polymerase. Physical Review Letters. 2008; 100

80. Banas P, Walter N, Sponer J, Otyepka M. Protonation States of the Key Active Site Residues and Structural Dynamics of the glmS Riboswitch As Revealed by Molecular Dynamics. Journal of Physical Chemistry B. 2010; 114:8701–8712.

81. Khavrutskii I, Grant B, Taylor SS, McCammon JA. A Transition Path Ensemble Study Reveals a Linchpin Role for Mg2+ during Rate-Limiting ADP Release from Protein Kinase A. Biochemistry. 2009; 48:11532–11545. [PubMed: 19886670]

82. Schulten K, et al. Scalable molecular dynamics with NAMD. Journal of Computational Chemistry. 2005; 26:1781–1802. [PubMed: 16222654]

83. Darden T, York D, Pedersen L. Particle Mesh Ewald - an N.Log(N) Method for Ewald Sums in Large Systems. Journal of Chemical Physics. 1993; 98:10089–10092.

84. Ryckaert J, Ciccotti G, Berendsen HJC. Numerical-Integration of Cartesian Equations of Motion of a System with Constraints - Molecular-Dynamics of N-Alkanes. Journal of Computational Physics. 1977; 23:327–341.

85. Brünger, AT. X-PLOR, Version 3.1 : a system for X-ray crystallography and NMR. Yale University Press; New Haven: 1992. p. xvii-382.

86. Feller S, Zhang Y, Pastor RW, Brooks BR. Constant-Pressure Molecular-Dynamics Simulation - the Langevin Piston Method. Journal of Chemical Physics. 1995; 103:4613–4621.

87. Martyna G, Tobias DJ, Klein ML. Constant-Pressure Molecular-Dynamics Algorithms. Journal of Chemical Physics. 1994; 101:4177–4189.

88. Hess B, Kutzner C, van der Spoel D, Lindahl E. GROMACS 4: Algorithms for highly efficient, load-balanced, and scalable molecular simulation. Journal of Chemical Theory and Computation. 2008; 4:435–447. [PubMed: 26620784]

89. Hess B, Bekker H, Berendsen HJC, Fraaije JGEM. LINCS: A linear constraint solver for molecular simulations. Journal of Computational Chemistry. 1997; 18:1463–1472.

90. Miyamoto S, Kollman PA. Settle - an Analytical Version of the Shake and Rattle Algorithm for Rigid Water Models. Journal of Computational Chemistry. 1992; 13:952–962.

91. Nose S. A Molecular-Dynamics Method for Simulations in the Canonical Ensemble. Molecular Physics. 1984; 52:255–268.

92. Hoover WG. Canonical Dynamics - Equilibrium Phase-Space Distributions. Physical Review A. 1985; 31:1695–1697. [PubMed: 9895674]

93. Parrinello M, Rahman A. Polymorphic Transitions in Single-Crystals - a New Molecular-Dynamics Method. Journal of Applied Physics. 1981; 52:7182–7190.

94. Nose S, Klein ML. Constant Pressure Molecular-Dynamics for Molecular-Systems. Molecular Physics. 1983; 50:1055–1076.

95. Liang J, Edelsbrunner H, Woodward C. Anatomy of protein pockets and cavities: Measurement of binding site geometry and implications for ligand design. Protein Science. 1998; 7:1884–1897. [PubMed: 9761470]

96. Le Guilloux V, Schmidtke P, Tuffery P. Fpocket: An open source platform for ligand pocket detection. Bmc Bioinformatics. 2009; 10

97. Patel A, Varilly P, Chandler D, Garde S. Quantifying Density Fluctuations in Volumes of All Shapes and Sizes Using Indirect Umbrella Sampling. Journal of Statistical Physics. 2011; 145:265–275. [PubMed: 22184480]

98. Baker N, Sept D, Joseph S, Holst MJ, McCammon JA. Electrostatics of nanosystems: Application to microtubules and the ribosome. Proceedings of the National Academy of Sciences of the United States of America. 2001; 98:10037–10041. [PubMed: 11517324]

99. Humphrey W, Dalke A, Schulten K. VMD: visual molecular dynamics. Journal of Molecular Graphics. 1996; 14:33–38. [PubMed: 8744570]

100. Loria J, Rance M, Palmer AG. A TROSY CPMG sequence for characterizing chemical exchange in large proteins. Journal of Biomolecular NMR. 1999; 15:151–155. [PubMed: 10605088]

101. Delaglio F, et al. NMRPipe: a multidimensional spectral processing system based on UNIX pipes. J Biomol NMR. 1995; 6:277–93. [PubMed: 8520220]

102. Johnson BA, Blevins RA. NMR View: A computer program for the visualization and analysis of NMR data. Journal of Biomolecular NMR. 1994; 4:603–614. [PubMed: 22911360]

103. Vranken WF, et al. The CCPN data model for NMR spectroscopy: development of a software pipeline. Proteins: Structure, Function, and Bioinformatics. 2005; 59:687–696.

104. Davis D, Perlman ME, London RE. Direct measurements of the dissociation-rate constant for inhibitor-enzyme complexes via the T1 rho and T2 (CPMG) methods. J Magn Reson B. 1994; 104:266–75. [PubMed: 8069484]

105. Carver J, Richards R. A general two-site solution for the chemical exchange produced dependence of T2 upon the Carr-Purcell pulse separation. Journal of Magnetic Resonance (1969). 1972; 6:89–105.

106. Jen J. Chemical exchange and NMR T2 relaxation—The multisite case. Journal of Magnetic Resonance (1969). 1978; 30:111–128.

107. Millet O, Loria J, Kroenke C, Pons M, Palmer AG III. The static magnetic field dependence of chemical exchange linebroadening defines the NMR chemical shift time scale. Journal of the American Chemical Society. 2000; 122:2867–2877.
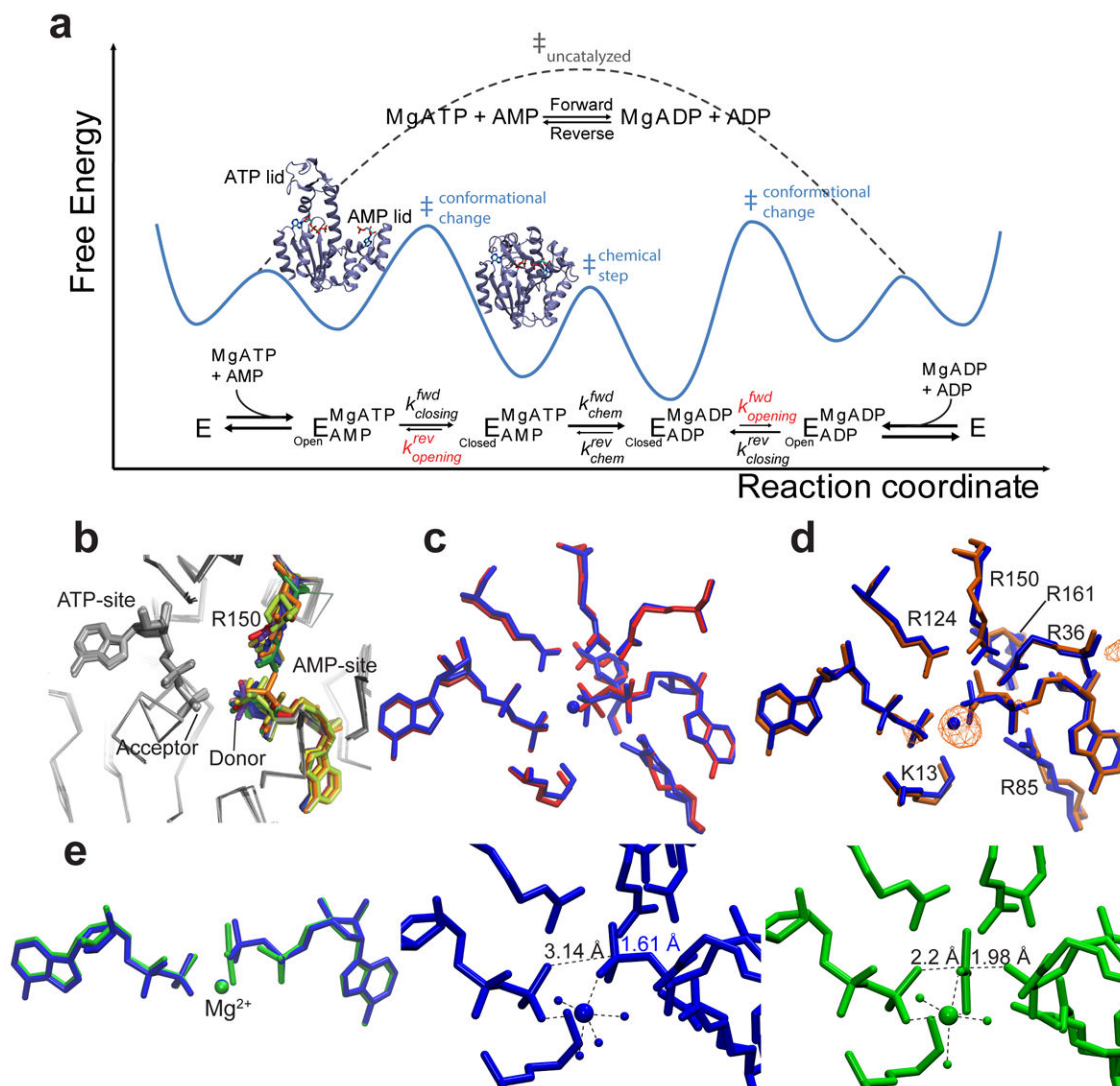
Figure 1. Adk free-energy landscape of catalysis and exploration of the phosphoryl-transfer step by X-ray crystallography

(a) Overall Adk reaction, minimal reaction scheme, and corresponding schematic of the catalytic energy landscape based on the measured enzyme kinetics (Table 2). Rate-limiting lid-opening ($k_{opening}$) is shown in red and visualized by the open and closed structures. (b) The superposition of AAdk structures with ADPs bound. Conformational heterogeneity of the donor phosphate group and R150 are highlighted in color. (c) Superposition of AAdk structures with bound ADPs in the presence (PDB 4CF7, blue) and absence (PDB 4JL5, red) of Mg^{2+}. (d) Superposition of AAdk complexed with Mg^{2+}–ADP–ADP (blue) and Co^{2+}–ADP–ADP (PDB 4JKY, orange). The anomalous scattering of the electron density at the Co-edge (λ=1.609 Å) is shown as anomalous difference map contoured at 5.5 σ (orange). (e) Superposition of Mg^{2+}–ADP–AMP–AlF_4^- (PDB 3SR0, green) with Mg^{2+}–ADP–ADP (blue). Detailed structures of the active site of both the substrate–enzyme complex (blue) and transition-state analogue (green) showing metal coordination and relevant O–P or O–Al distances (dashed lines) and the covalent O–P bond (blue).
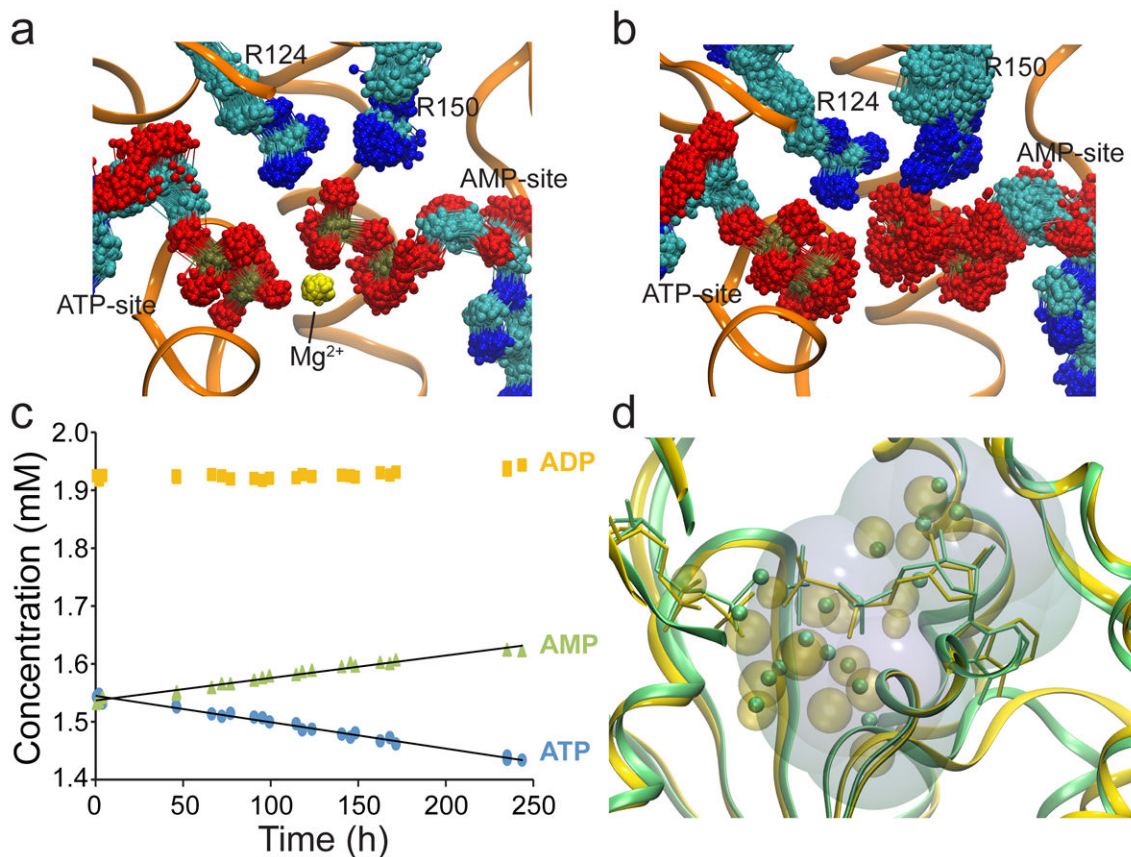
Figure 2. Role of active-site dynamics in efficient phosphoryl transfer versus unproductive hydrolysis

(a,b) Superposition of representative snapshots of 200 ns MD simulations of the ADP–ADP ternary complex of AAdk (a) with (yellow) and (b) without Mg^{2+}. **(c)** Unproductive ATP hydrolysis by 100 μM of EAdk. Fit of the time dependence of nucleotide concentrations yielded a hydrolysis rate of $\sim 2 \circ 10^{-6}$ s^{-1}. **(d)** Overlay of the active site of the crystal structure of AAdk bound to Mg^{2+}–ADP–AMP–AlF_4^- (green) including bound water molecules (green spheres) and a typical snapshot from a 200 ns MD simulation of the AAdk–Mg^{2+}–ADP–ADP complex (yellow). The transparent yellow spheres represent the isosurface of value 0.75 for the fractional occupancy of the water oxygen atoms during the MD simulation. A cavity excluded from access to bulk solvent (transparent green) is solvated by a number of water molecules.
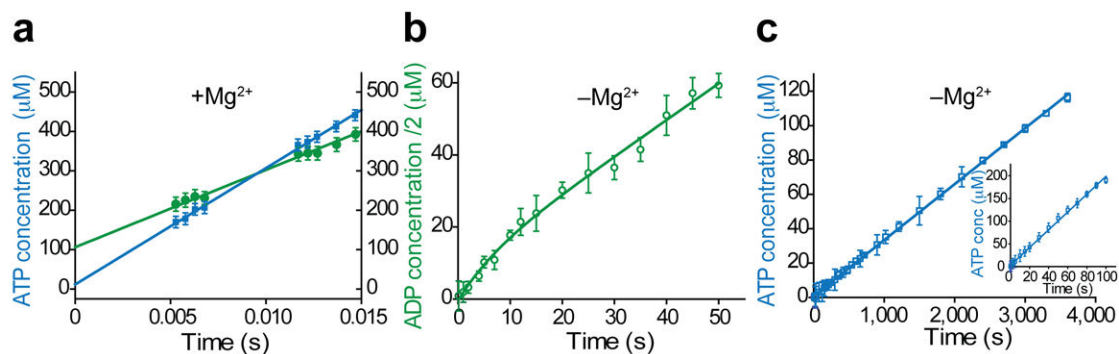
Figure 3. Catalytic effect of the Mg^{2+} cofactor
Pre-steady-state kinetics of EAdk at 25 °C measured by quench-flow **(a)** with and **(b,c)** without Mg^{2+} (*n* = 3 experiments; mean ± s.e.m.). **(a)** 113 μM EAdk, 4 mM ATP, 4 mM AMP and 8 mM MgCl$_2$ in the forward direction (green) and 4 mM ADP and MgCl$_2$ in the reverse direction (blue) were used. **(b)** A resolved burst phase is seen in the forward direction with 20 μM EAdk and 4 mM ATP and AMP, providing the rates of both the P-transfer and lid-opening, while in the reverse reaction **(c)** No burst phase is seen with 20 μM or 500 μM EAdk (inset) and 4 mM ADP.
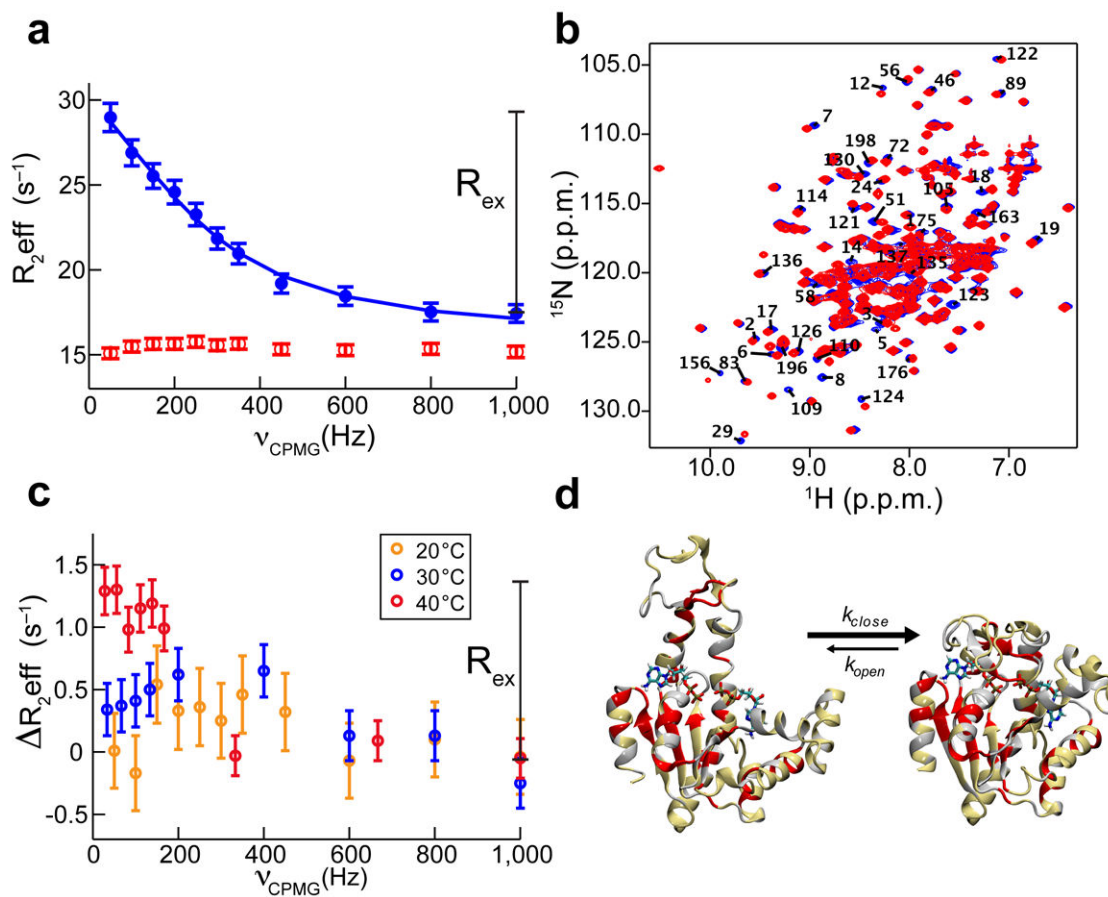
Figure 4. EAdk structure and dynamics during catalysis with and without Mg^{2+} studied by NMR

(a) ^{15}N-TROSY CPMG relaxation dispersion NMR experiments at 25 °C on WT EAdk saturated with 20 mM nucleotides. Representative dispersion profile for residues sensitive to lid-opening/closing in the presence of Mg^{2+} (blue) are fully suppressed in its absence (red). **(b)** Overlay of [^1H-^{15}N]-TROSY-HSQC spectra of WT EAdk during turnover with (blue) and without (red) Mg^{2+}. **(c)** Temperature dependence of normalized ^{15}N-TROSY CPMG relaxation dispersion profiles of WT EAdk. **(d)** Residues with dispersion curves at 40 °C without Mg^{2+} are plotted on the EAdk–ADP–ADP open and closed structures (red); residues with no data due to overlap or missing signals are shown in grey and nucleotides are shown in stick representation. Uncertainties (s.d.) in R_{2eff} (a,c) were estimated from the variance for a number of non-exchanging peaks (n = 7).
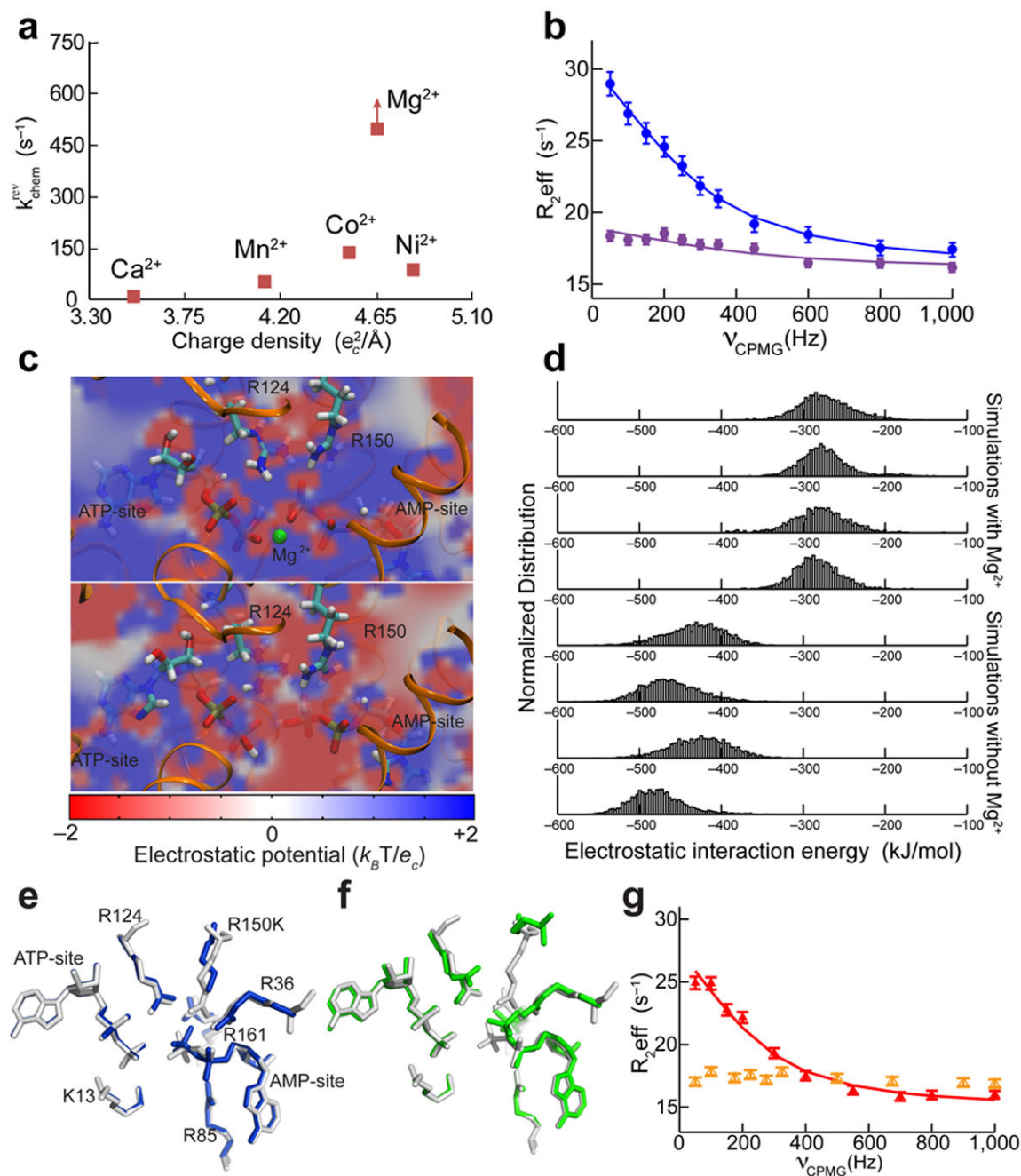
Figure 5. The nature of the divalent cation drastically affects phosphoryl transfer but not Adk conformational dynamics

(a) The P-transfer step of EAdk in the reverse reaction measured as a function of different divalent metals. The rate constant shown for Mg^{2+} is a lower limit. **(b)** ^{15}N-TROSY CPMG relaxation dispersion profiles of EAdk with Mg^{2+} (blue) or Ca^{2+} (purple). **(c)** Active-site electrostatic potential computed from representative structures extracted from the MD simulations with (top) or without (bottom) Mg^{2+}, plotted on a plane cutting through the active site. **(d)** The distribution of the electrostatic interaction energy between the ADP molecules and R124 and R150 is plotted for four MD simulations with and without Mg^{2+}.

The histograms show the electrostatic interaction energies computed for configurations evenly distributed in time along the trajectories. **(e,f)** The two molecules in the asymmetric unit of AAdk R150K with ADP bound (blue and green) are superimposed with WT AAdk (gray). **(g)** ^{15}N-TROSY CPMG relaxation dispersion at 25 °C on the EAdk R150K mutant saturated with 20 mM nucleotides. Dispersion curves for residues sensitive to lid-opening/closing in the presence of Mg^{2+} (red) are fully suppressed in the absence of Mg^{2+} (orange). Uncertainties (s.d.) in R_{2eff} (b,g) were estimated from the variance for a number of non-exchanging peaks (n = 7).

Table 1

Data collection and refinement statistics

	AAdk1 ADP–ADP	AAdk2 ADP–ADP	AAdk3 ADP–ADP	AAdk4 ADP–ADP	AAdk5 AMPPN–AMPPN	AAdk6 ADP–ADP
Data collection						
Space group	P212121	P212121	P212121	P212121	P212121	P212121
Cell dimensions						
a, b, c (Å)	66.17,69.56, 85.39	66.64,70.54, 85.88	67.00,73.73, 87.52	67.00,74.72, 88.15	66.47, 71.56, 86.30	66.94, 73.89, 87.80
α, β, γ (°)	90, 90, 90	90, 90, 90	90, 90, 90	90, 90, 90	90, 90, 90	90, 90, 90
Resolution (Å)	29.0–1.24 (1.31–1.24)	42.9–1.55 (1.64–1.55)	37.6–1.53 (1.61–1.53)	38.0–1.79 (1.88–1.79)	43.2–1.65 (1.74–1.65)	43.9–2.12 (2.23–2.12)
R_{merge}	0.062 (0.427)	0.139 (1.287)	0.072 (1.342)	0.105 (0.566)	0.065 (0.653)	0.174 (1.698)
$I / \sigma I$	22.1 (5.7)	8.1 (1.4)	18.8 (1.9)	14.5 (3.2)	11.9 (2.0)	7.8 (1.8)
Completeness (%)	99.4 (96.2)	97.6 (93.5)	100.0 (99.8)	100.0 (100.0)	99.1 (98.0)	91.1 (99.9)
Redundancy	14.0 (12.1)	11.5 (9.4)	14.0 (13.3)	12.0 (9.3)	6.8 (6.2)	6.5 (6.8)
Refinement						
Resolution (Å)	29.0–1.24	36.1–1.55	36.6–1.53	38.0–1.79	42.4–1.65	43.9–2.12
No. reflections	111278	57161	62870	42421	49227	22909
R_{work} / R_{free}	0.130/0.159	0.185/0.229	0.173/0.232	0.180/0.232	0.208/0.241	0.186/0.256
No. atoms						
Protein	7181	3360	3306	3386	3365	3256
Ligand/ion	195	108	108	108	108	108
Water	797	471	510	644	361	227
B-factors						
Protein	16.1	24.6	28.1	21.5	33.5	39.2
Ligand/ion	9.7	18.7	21.2	16.7	26.0	31.4
Water	26.7	37.6	38.2	31.8	40.6	37.8
r.m.s. deviations						
Bond lengths (Å)	1.501	1.215	1.204	1.234	1.237	1.234
Bond angles (°)	0.010	0.006	0.005	0.007	0.007	0.008

	AAdk7 Co²⁺–ADP–ADP	AAdk8 Mg²⁺–ADP–AMP–AlF₄⁻	AAdk9 R150K	AAdk10 R150K	AAdk11 Mg²⁺–ADP–ADP
Data collection					
Space group	P2₁2₁2₁	P2₁2₁2₁	P2₁2₁2₁	P2₁2₁2₁	P2₁2₁2₁
Cell dimensions					
a, b, c (Å)	67.55, 73.53, 87.47	65.95, 69.58, 85.67	67.17, 71.01, 85.83	67.01, 70.46, 85.58	64.09, 64.70,86.26
α, β, γ (°)	90, 90, 90	90, 90, 90	90, 90, 90	90, 90, 90	90, 90, 90
Resolution (Å)	56.3–2.37 (2.50–2.37)	41.8–1.57 (1.65–1.57)	48.8–1.73 (1.82–1.73)	36.6–1.43 (1.51–1.43)	64.7–1.59 (1.64–1.59)
R_{merge}	0.062 (0.198)	0.085 (0.310)	0.054 (0.123)	0.053 (0.268)	0.088 (0.622)
$I / \sigma I$	25.6 (9.8)	11.9 (3.7)	18.1 (6.5)	17.5 (4.3)	12.2 (3.1)
Completeness (%)	99.7 (97.9)	99.7 (98.3)	99.9 (100.0)	99.9 (99.8)	100.0 (100.0)
Redundancy	13.5 (12.7)	6.4 (4.8)	6.4 (5.0)	6.7 (5.1)	6.5 (6.7)
Refinement					
Resolution (Å)	53.5–2.37	41.8–1.57	42.4–1.73	36.1–1.43	40.3–1.59
No. reflections	17150	56016	43855	74937	48566
R_{work} / R_{free}	0.199/0.267	0.148/0.189	0.161/0.210	0.153/0.195	0.182/0.216
No. atoms					
Protein	3245	6995	3367	3365	3300
Ligand/ion	110	160	108	108	159
Water	144	759	518	703	335
B-factors					
Protein	42.0	16.0	21.1	20.0	20.5
Ligand/ion	34.0	10.6	15.6	14.8	14.0
Water	37.4	28.1	32.7	33.6	28.0
r.m.s. deviations					
Bond lengths (Å)	1.276	1.515	1.222	1.253	1.328
Bond angles (°)	0.008	0.014	0.006	0.005	0.007

The number of crystals for each structure is one.

Table 2

Microscopic rate constants for EAdk catalysis

	metal		P-transfer		Lid-opening	
			forward $E^{ATP}_{AMP} \rightarrow E^{ADP}_{ADP}$	**reverse** $E^{ADP}_{ADP} \rightarrow E^{ATP}_{AMP}$	**forward** E^{ADP}_{ADP}	**reverse** E^{ATP}_{AMP}
WT	none		0.14 ± 0.1 [a]	0.005 ± 0.003 [a]	0.05 ± 0.01 [a],[*]	0.09 ± 0.05 [a]
	Mg^{2+}		>5000 [c]	>500 [b]	190 ± 30 [d],[**]	2800 ± 200 [d]
	Ca^{2+}		>500 [b]	24 ± 4 [e]	260 ± 30 [d],[***]	>2600 [f]
	Co^{2+}		>500 [b]	150 ± 15 [e]	190 ± 20 [d]	>1900 [f]
R150K	none		$(4.6 \pm 0.2)°10^{-5}$ [e]	$(6.5 \pm 1.2)°10^{-6}$ [e]	<1 [g]	<1 [g]
	Mg^{2+}		0.7 ± 0.2 [e]	0.5 ± 0.1 [e]	300 ± 75 [g]	

[a] from the observed forward and reversed rates from quench-flow data and on-enzyme equilibrium.

[b] lower limit determined from the burst within the dead time of the quench-flow instrument (~5 ms).

[c] lower limit from the quench-flow dead time and on-enzyme equilibrium

[d] from the steady-state (linear) phase of the quench-flow experiment and on-enzyme equilibrium.

[e] from the linear phase of the quench-flow experiment.

[f] calculated from $k_{cat,obs}$ and probability to be in the corresponding states.

[g] from NMR relaxation dispersion data.

[*] in good agreement with upper limit established by NMR (<1 s^{-1}).

[**] in good agreement with NMR value of 210 ± 80 s^{-1}.

[***] in good agreement with NMR value of 370 ± 140 s^{-1}.